NANO · MICRO small
www.small-journal.com

An Ultra-Stable Electrode-Solid Electrolyte Composite for High-Performance All-Solid-State Li-Ion Batteries

Yuqin Huang, Panyu Gao, Tengfei Zhang, Xiang Zhang, Guanglin Xia, Fang Fang, Dalin Sun, Zaiping GuoProf.,* and Xuebin YuProf.**

The low ionic and electronic conductivity between current solid electrolytes and high-capacity anodes limits the long-term cycling performance of all-solid-state lithium-ion batteries (ASSLIBs). Herein, this work reports the fabrication of an ultra-stable electrode-solid electrolyte composite for high-performance ASSLIBs enabled by the homogeneous coverage of ultrathin $Mg(BH_4)_2$ layers on the surface of each MgH_2 nanoparticle that are uniformly distributed on graphene. The initial discharge process of $Mg(BH_4)_2$ layers results in uniform coverage of MgH_2 nanoparticle with both $LiBH_4$ as the solid electrolyte and Li_2B_6 with even higher Li ion conductivity than $LiBH_4$. Consequently, the Li ion conductivity of graphene-supported MgH_2 nanoparticles covered with ultrathin $Mg(BH_4)_2$ layers is two orders of magnitude higher than that without $Mg(BH_4)_2$ layers. Moreover, the thus-formed inactive Li_2B_6 with strong adsorption capability toward $LiBH_4$, acts as a stabilizing framework, which, coupled with the structural support role of graphene, alleviates the volume change of MgH_2 nanoparticles and facilitates the intimate contact between $LiBH_4$ and individual MgH_2 nanoparticles, leading to the formation of uniform stable interfaces with high ionic and electronic conductivity on each MgH_2 nanoparticles. Hence, an ultrahigh specific capacity of 800 mAh g^{-1} is achieved for MgH_2 at 2 A g^{-1} after 350 cycles.

1. Introduction

During the extensive application of portable electronic devices and electric vehicles, the concerns of energy density and safety issues of current Li-ion batteries (LIBs) due to the combustible nature and limited electrochemical window of organic electrolytes attract ever-growing attentions.[1,2] As a result, all-solid-state LIBs (ASSLIBs) that uses solid electrolytes with inflammability and wide electrochemical windows are believed to be an excellent candidate for future energy storage systems.[3–6] Unfortunately, unlike conventional LIBs that uses a permeable liquid electrolyte to soak the whole electrode, the uniform distribution of solid electrolytes within the electroactive materials is difficult to realize in ASSLIBs due to their poor rigid solid-solid contact, which leads to the presence of large interfacial resistance and low interfacial compatibility between solid electrolytes and the electrodes.[7–9] Therefore, despite tremendous research advancements in solid electrolytes, their practical application, however, is still in its infancy, mainly in terms of energy density, and hence effective strategies that could homogeneously combine suitable high-energy-density electrodes with solid electrolytes should be developed.

In this regard, metal hydrides are one of the most promising anodes for building high energy-density ASSLIBs due to their high theoretical capacity (e.g., 2032 mAh g^{-1} for MgH_2) and low electrochemical potential.[10–13] Moreover, compared with all other conversion anodes, the lowest value of polarization has been ever reported for MgH_2 as the anode material due to the facile transportation of hydrogen toward the reversible lithiation and delithiation of MgH_2.[14–16] Among all the reported solid electrolytes, lithium borohydride ($LiBH_4$) is a potential candidate for use as the solid electrolyte for assembling ASSLIBs with high energy density owing to its wide electrochemical stability window and the stable compatibility with MgH_2-based anodes.[17–21] In addition, the hydrogen exchange effect between $LiBH_4$ and MgH_2 could facilitate H^- conductivity inside the electrode, which is able to further promote the reversibility of MgH_2 for Li storage performance.[22,23] The reversible Li storage reaction of MgH_2, however, is significantly limited by the insulating nature of MgH_2 and the large volume change involved during its conversion reaction. Such issues have been solved to some extent by building nanostructured MgH_2 anode that are uniformly distributed on electronic conductive carbon, which could simultaneously alleviate the volume change of MgH_2 anode and increase the electronic conductivity of the whole

Y. Huang, P. Gao, G. Xia, F. Fang, D. Sun, X. Yu
Department of Materials Science
Fudan University
Shanghai 200433, China
E-mail: xiaguanglin@fudan.edu.cn; yuxuebin@fudan.edu.cn
T. Zhang, X. Zhang
College of Materials Science and Technology
Nanjing University of Aeronautics and Astronautics
Nanjing, Jiangsu 210016, China
Z. Guo
School of Chemical Engineering and Advanced Materials
The University of Adelaide
Adelaide, South Australia 5005, Australia
E-mail: zaiping.guo@adelaide.edu.au
The ORCID identification number(s) for the author(s) of this article can be found under https://doi.org/10.1002/smll.202207210.

DOI: 10.1002/smll.202207210

 © 2023 Wiley-VCH GmbH

electrode.[22,24,25] Unfortunately, the electrochemical activity of MgH_2 still suffers from the large electrode/electrolyte interfacial resistance, induced by the intrinsic poor solid-solid contact between MgH_2 and $LiBH_4$ due to their intrinsic nonfluidity and rigidity. Moreover, the volume change of MgH_2 during lithiation and delithiation process would accelerate the detachment of MgH_2 from the solid-electrolyte and hence the loss of electrochemical activity of MgH_2, resulting in fast deterioration of reversible Li storage capacity. Thus, building homogeneous solid-state MgH_2 anodes with stable interfaces that have high ionic and electronic conductivity poses a key challenge in realizing their practical applications in ASSLIBs with high energy density.

Herein, we report the construction of ionic conductive pathways on MgH_2 nanoparticles (NPs) which are uniformly connected by electronic conductive graphene to trigger the electrochemical activity of MgH_2 with ultra-stable reversibility in ASSLIBs. It is realized by the uniform coverage of each MgH_2 NP with ultrathin $Mg(BH_4)_2$ layers (denoted as MH@MBH NPs) through in situ reaction between MgH_2 NPs and diborane. The homogeneous distribution of MH@MBH NPs on graphene not only increases the interfacial electronic conductivity of the whole electrode but also decreases the Li ion diffusion pathways during reversible charge and discharge process. More importantly, the thus-formed ultrathin $Mg(BH_4)_2$ layers would be in situ transformed into solid electrolyte $LiBH_4$ and Li_2B_6 in the initial discharge process, uniformly covered on the surface of each MgH_2 NP. Interestingly, it is theoretically demonstrated that Li_2B_6 exhibits a Li ion diffusion barrier even lower than that of $LiBH_4$, leading to Li ion conductivity two orders of magnitude higher than the sample without $Mg(BH_4)_2$ coating. In addition, the binding energy between Li_2B_6 and $LiBH_4$ reaches 1.48 eV, much higher than that of MgH_2 (0.26 eV), which demonstrates the strong adsorption capability of Li_2B_6 toward $LiBH_4$. Hence, the thus-formed inactive Li_2B_6 could serve as a stable framework, which, coupled with the structural support role of graphene, not only alleviates the volume change of MgH_2 NPs but also stabilizes the intimate contact between $LiBH_4$ and individual MgH_2 NPs, resulting in stable interfaces with high ionic and electronic conductivity on each MgH_2 NPs uniformly connected by graphene. As a result, a specific capacity of 800 mAh g^{-1} is achieved for MgH_2 anode modified by ultrathin $Mg(BH_4)_2$ layers in ASSLIBs at a high current density of 2 A g^{-1} after 350 cycles.

2. Results and Discussion

The synthesis procedure of MgH_2 NPs decorated with ultrathin $Mg(BH_4)_2$ layers is schematically illustrated in **Figure 1**. First, graphene-supported MgH_2 NPs (denoted as MHG) are fabricated based on hydrogenation-induced self-assembly of $(C_4H_9)_2Mg$, in which the facile control over the particle size of MgH_2 NPs that are uniformly distributed on graphene with high purity that could be verified by Raman spectrum (Figure S1, Supporting Information) could be realized by changing the amount of solvent of $(C_4H_9)_2Mg$ (Figure S2, Supporting Information).[26–28] Subsequently, taking advantage of MHG as the nanoreactor for in situ solid-gas reaction between MgH_2 NPs and B_2H_6,[29] in which the graphene with flexible and porous structure not only acts as the structural support to inhibit the aggregation and growth of MgH_2 NPs, but also provides facile pathways for the transportation of B_2H_6 to promote the uniform reaction with MgH_2 NPs, a layer of $Mg(BH_4)_2$ shell could be constructed on the surface of each MgH_2 NP. MgH_2 NPs homogeneously distributed on graphene with the average size of 47.7 (denoted as MHG-50, Figure S3, Supporting Information) and 11.6 nm (denoted as MHG-13, Figure S4, Supporting Information) are synthesized respectively for comparison and characterization, which results in the formation of MH@MBH NPs on graphene with the average size of 13 (denoted as MHG@MBH-13) and 49.6 nm (denoted as MHG@MBH-50), respectively. Considering the increase of the average particle size (Figure S5, Supporting Information), the thickness of the as-synthesized $Mg(BH_4)_2$ shell could be calculated to be ≈0.7 and 1.0 nm for MHG@MBH-13 and MHG@MBH-50, respectively. Scanning electron microscopy (SEM) and transmission electron microscopy (TEM) images validate that, owing to the presence of graphene as the robust structural support, the homogeneous distribution of MgH_2 NPs on graphene are well preserved after this in situ solid-gas reaction (**Figure 2**). Moreover, the characteristic lattice fringes of 0.43 nm, corresponding to the (100) plane of $Mg(BH_4)_2$, could be clearly observed on the surface of MgH_2 NPs that exhibit its typical lattice fringes of 0.23 nm of the (200) plane (Figure 2d), indicating the successful coating of $Mg(BH_4)_2$ on MgH_2 NPs.

Interestingly, scanning TEM (STEM) image reveal that original MgH_2 NPs break up into several smaller NPs inside of the layer of $Mg(BH_4)_2$ (Figure 2e,f) attributed to the Kirkendall effect that leads to the simultaneous formation of $Mg(BH_4)_2$ as the shell and the porous structure of MgH_2 inside.[30] The void spaces between MgH_2 nanocrystals inside of the shell are capable of alleviating the volume expansion of MgH_2 NPs during cycling charge and discharge process, while the cracked MgH_2 NPs provide more active sites and shorter diffusion pathway. The elemental line-scan profile of single MH@MBH NPs illustrates the higher intensity of signal B in the fringe of MgH_2 NPs than the center area (Figure 2e), indicating the uniform coverage of MgH_2 NPs by $Mg(BH_4)_2$ layers, which provides additional evidence to the formation of yolk-shell-like structure. Elemental mapping results confirm that the distribution of Mg, B, and C elements matches well with each other, further demonstrating the uniform formation of the $Mg(BH_4)_2$ shell on the surface of MgH_2 NPs (Figure 2g).

Although the characteristic XRD peaks of β-MgH_2 are clearly weakened and broadened in the as-prepared MBH@MH after the reaction between MgH_2 and B_2H_6 attributed to the decrease of particle size of MgH_2 NPs and the uniform coverage of $Mg(BH_4)_2$, no characteristic peaks of $Mg(BH_4)_2$ could be detected (Figure S6, Supporting Information), indicating its amorphous nature. Fortunately, the formation of $Mg(BH_4)_2$ could be verified by the presence of its characteristic peak at 2400 cm^{-1} in Raman spectra (Figure S7a,b, Supporting Information) and the strong peaks at ≈2300 and 1175 cm^{-1} assigned to the stretching of B—H bonds of $Mg(BH_4)_2$ in fourier-transform infrared (FTIR) spectra (Figure S7c, Supporting Information). The broad peaks at ≈1338 and 1600 cm^{-1} of all the as-synthesized MH@MBH in Raman spectra could be indexed to typical *D*

 © 2023 Wiley-VCH GmbH

16136829, 2023, 26, Downloaded from https://onlinelibrary.wiley.com/doi/10.1002/smll.202207210 by Fudan University, Wiley Online Library on [28/06/2023]. See the Terms and Conditions (https://onlinelibrary.wiley.com/terms-and-conditions) on Wiley Online Library for rules of use; OA articles are governed by the applicable Creative Commons License

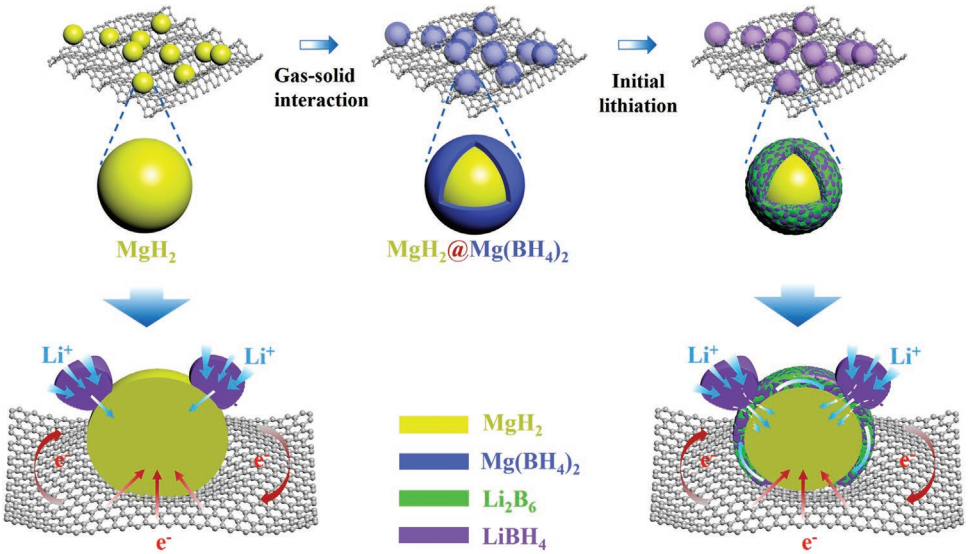

Figure 1. Schematic illustration of the preparation procedure of MH@MBH NPs distributed on the surface of graphene and the construction of high ionic and electronic conductivity on each MgH_2 NP uniformly connected by graphene.

and *G* bands of graphene. The Brunauer–Emmett–Teller (BET) surface of MHG@MBH-13 is calculated to be 150.8 m^2 g^{-1} with a pore size distribution from 2 to 30 nm, which provides additional evidence to the mesoporous structure (Figure S7d, Supporting Information). The loading amount of MgH_2 is calculated to be ≈60% for both MHG-50 (Figure S8, Supporting Information) and MHG-13 (Figure S9, Supporting Information) based on their respective hydrogen desorption capacity.

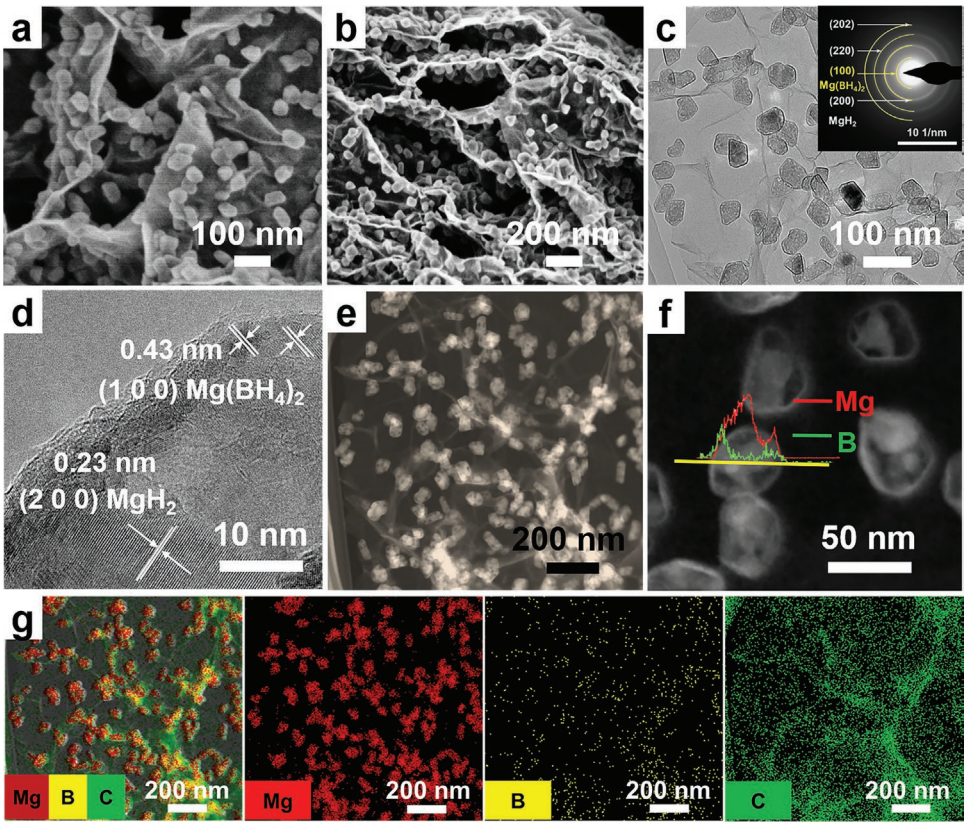

Figure 2. a,b) SEM images, c) TEM images, and the d) HRTEM images of MHG@MBH-50. e) The EDS line scan of MH@MBH nanocrystals on a STEM image and the corresponding element distributions of f) Mg and B. g) The STEM image and the corresponding elemental mapping of Mg, B, and C for MHG@MBH-50. The inset of (c) is the corresponding SAED patterns of the as-prepared MHG@MBH-50.

 © 2023 Wiley-VCH GmbH

16136829, 2023, 26, Downloaded from https://onlinelibrary.wiley.com/doi/10.1002/smll.202207210 by Fudan University, Wiley Online Library on [28/06/2023]. See the Terms and Conditions (https://onlinelibrary.wiley.com/terms-and-conditions) on Wiley Online Library for rules of use; OA articles are governed by the applicable Creative Commons License

In addition, in comparison to MHG-13, an obvious increase of hydrogen desorption capacity could be observed for MHG@MBH-13 due to the formation of $Mg(BH_4)_2$ with higher hydrogen storage capacity than MgH_2 (Figure S10, Supporting Information). No contamination of Zn could be observed for the as-synthesized MHG@MBH-13 (Figure S11, Supporting Information).

The electrochemical performance of MH@MBH NPs with various particle sizes is first investigated in ASSLIBs using Li foils as the counter electrode at a current density of 0.2 A g^{-1}, with the respective graphene-supported MgH_2 NPs included for comparison. As shown in Figure S12, Supporting Information, only a specific capacity of 850 mAh g^{-1} could be obtained for pure MgH_2 NPs with an average particle size of 50 nm on graphene after 10 cycles while this value is significantly increased to 1000 mAh g^{-1} after the uniform coating of $Mg(BH_4)_2$, indicating the effective role of $Mg(BH_4)_2$ in improving the electrochemical activity of MgH_2. Particularly, upon decreasing the particle size of MgH_2 NPs down to 13 nm, an ultrahigh specific capacity of 1700 mAh g^{-1} could be achieved for MHG@MBH-13 under the identical condition, which is the best among all the as-synthesized MH@MBH NPs. As a result, MHG@MBH-13 is selected for subsequent investigation in detail. It should be noted that the electrochemical performance of the used graphene and the conductive carbon was also measured under identical test conditions (Figure S13, Supporting Information). It was confirmed that these electrodes contributed negligibly to Li^+ storage (i.e., 20 mAh g^{-1} for the conductive carbon and 67 mAh g^{-1} for the graphene). The galvanostatic discharge and charge curves of MHG@MBH-13 indicates that an initial discharge capacity of 2054 mAh g^{-1}, which is comparable to the theoretical capacity of MgH_2, could be obtained (**Figure 3**a). More importantly, a reversible charge capacity of 2015 mAh g^{-1} could be delivered at the first cycle, corresponding to an ultrahigh initial CE of 98%, which confirms the excellent reversibility of MHG@MBH-13. In contrast, an initial CE of only 84% can be obtained for MHG-13 with an initial charge capacity of 1656 mAh g^{-1} (Figure S14, Supporting Information). In addition to the first cycle, the galvanostatic discharge and charge curves of MHG@MBH-13 of initial three cycles and their differential curves are almost overlapped completely, providing additional evidence to the stable reversibility of MHG@MBH-13. In strong contrast, continuous decay of the discharge and charge peak intensity along with the proceeding of cycling process is observed for MHG-13. The peak located at ≈0.45 V in the first discharge process of MHG@MBH-13 could be attributed to the reduction of MgH_2 with the formation of LiH as the by-product, whereas the initial charge peak at ≈0.55 V could be attributed to the extraction of Li and the regeneration of MgH_2 (Figure 3b). Another pair of weak redox peaks at 0.85/1.16 V that has also been detected in previously published results[22] could be observed, which could be attributed to the reversible formation of solid electrolyte interphase. Upon the proceeding of the charge and discharge process, the reversible specific capacity of MHG-13 is rapidly decreased to only 897 mAh g^{-1} after 150 cycles (Figure 3c), whereas an ultrahigh specific capacity of 1498 mAh g^{-1}, corresponding to a capacity retention of 88% to that of the tenth cycle, could be obtained for MBH@MH-13 under identical condition. Interestingly, MHG@MBH-13 without the addition of conductive carbon only delivered a specific capacity of 408 mAh g^{-1} after 47 cycles and this value could be increased to 915 mAh g^{-1} after the addition of conductive carbon with a weight ratio of 30% in the electrode of MHG@MBH-13 (Figure S15, Supporting Information). This result indicates the positive role of conductive carbon in enhancing the electrochemical performance of MHG@MBH-13, which could be induced by the high electrical conductivity of Ketjen black that is able to improve the electrical conductivity of the thus-fabricated electrode.

Rate performance demonstrates that a reversible capacity of 1652, 1495, 1345, 1228, and 1080 mAh g^{-1} could be achieved for MHG@MBH-13 at the current density of 0.1, 0.2, 0.5, 1, and 2 A g^{-1}, respectively, much higher than that of MHG-13 (Figure 3d). When the current density is reduced back to 100 mA g^{-1}, a high specific capacity of 1566 mAh g^{-1} could be retained for MHG@MBH-13 with nearly no capacity fading, validating the strong tolerance of MHG@MBH-13 toward fast charge and discharge process. Upon cycling at 1 A g^{-1}, a reversible specific capacity of 1318 mAh g^{-1} could be maintained for MHG@MBH-13 after 350 cycles (Figure 3e). Impressively, upon further increasing the current density to 2 A g^{-1}, MHG@MBH-13 is still able to deliver a reversible capacity of 800 mAh g^{-1} after 350 cycles (Figure 3f). By comparison, the specific capacity of MHG-13 is degraded to 575 mAh g^{-1} after only 200 cycles. These results directly demonstrate the positive role of uniform coating of $Mg(BH_4)_2$ in improving the electrochemical activity of MgH_2.

XRD results of MHG@MBH-13 at various states reveal the formation of Mg and LiH upon the discharge process with complete disappearance of MgH_2 and reversible regeneration of MgH_2 after the charge process (**Figure 4**a,b), demonstrating the excellent reversibility of MgH_2. No signals belonging to $Mg(BH_4)_2$, however, could be detected during the whole charge and discharge process, which indicates the amorphous nature of thus-formed $Mg(BH_4)_2$ layers and/or its decomposed products. Therefore, in order to unravel the role of $Mg(BH_4)_2$ in enhancing Li storage performance of MgH_2, the electrochemical activity of pristine $Mg(BH_4)_2$ is investigated in detail. After the discharge process of $Mg(BH_4)_2$, Mg as verified by XRD results (Figure S16, Supporting Information) and $LiBH_4$ as verified by solid-state NMR results (Figure S17, Supporting Information) could be confirmed, which verifies the lithiation reaction of $Mg(BH_4)_2$ according to the equation, that is, $Mg(BH_4)_2 + 2Li \rightarrow Mg + 2LiBH_4$, corresponding to a theoretical capacity of 993 mAh g^{-1}.[29] This value, however, is much lower than the experimentally observed discharge capacity of bulk $Mg(BH_4)_2$ (i.e., 1680 mAh g^{-1}, Figure S18, Supporting Information). Interestingly, upon reducing the particle size of $Mg(BH_4)_2$ down to 10 nm, graphene-supported $Mg(BH_4)_2$ NPs (denoted as $Mg(BH_4)_2$@G) via the gas-solid reaction between graphene-supported MgH_2 NPs and diborane delivers an ultrahigh discharge capacity of 2750 mAh g^{-1} (Figure S19, Supporting Information), indicating the possible formation of B from the lithiation of $Mg(BH_4)_2$ NPs followed by the lithiation of B as verified previously by the theoretical calculation (Table S1, Supporting Information), which contributes to the significant increase of Li storage capacity (Figure S20, Supporting Information). The lithiation of amorphous B could be further

© 2023 Wiley-VCH GmbH

16136829, 2023, 26, Downloaded from https://onlinelibrary.wiley.com/doi/10.1002/smll.202207210 by Fudan University, Wiley Online Library on [28/06/2023]. See the Terms and Conditions (https://onlinelibrary.wiley.com/terms-and-conditions) on Wiley Online Library for rules of use; OA articles are governed by the applicable Creative Commons License

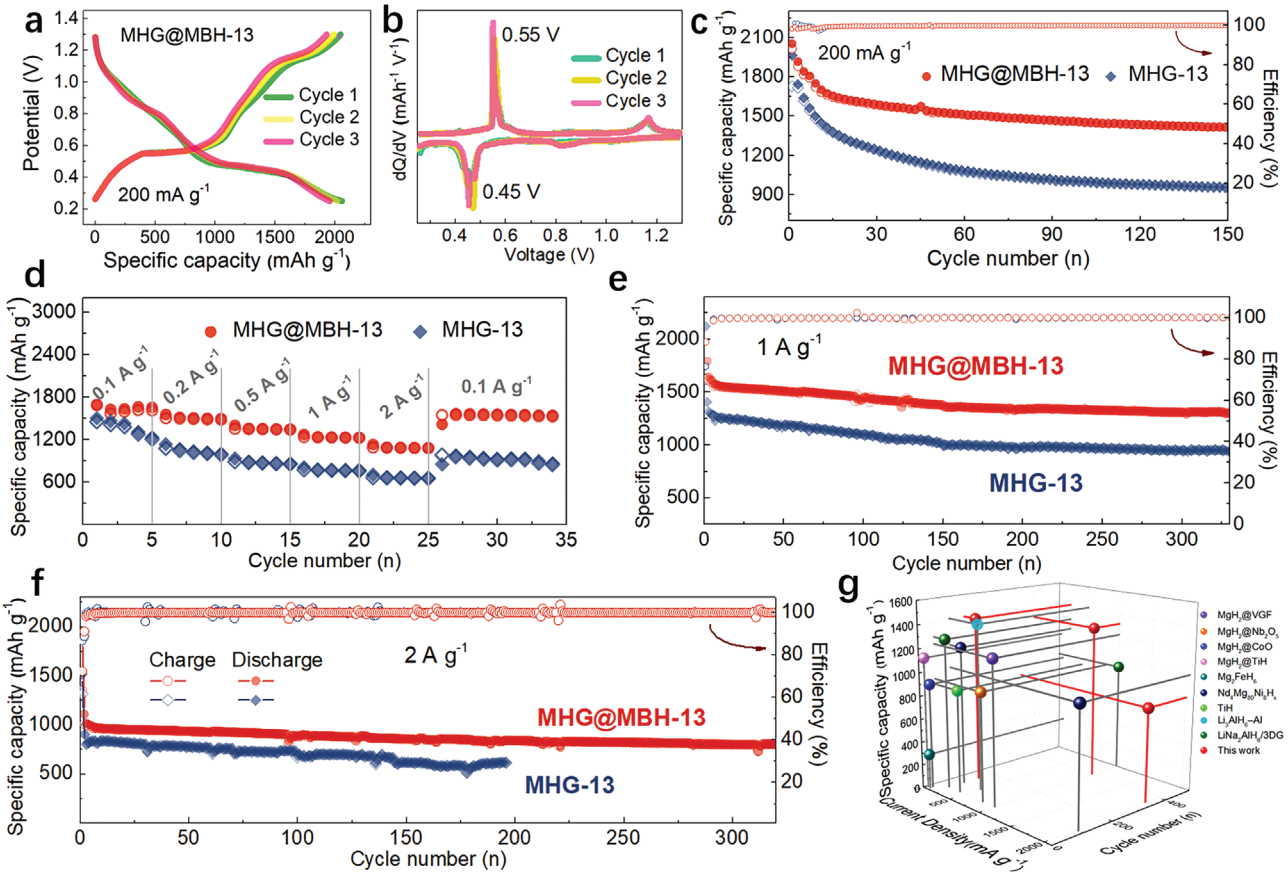

Figure 3. a) Galvanostatic charge–discharge profiles of MHG@MBH-13 at 200 mA g^{-1} and b) its corresponding derivative curves (dQ/dE). c) Cycling performance of MHG@MBH-13 and MHG electrodes at 200 mA g^{-1}. d) Rate performance of MHG@MBH-13 and MHG-13 electrodes at various current densities from 100 mA g^{-1} to 2 A g^{-1}. e,f) Cycling performance of MHG@MBH-13 and MHG-13 electrodes at 1 and 2 A g^{-1}. g) Comparison of cycling charge and discharge performance of the as-prepared MHG@MBH-13 electrode and previously reported metal hydride-based anodes in all-solid-state batteries.

supported by XRD (Figure S21, Supporting Information) and XPS results (Figure S22, Supporting Information), which, however, would lead to the irreversible formation of Li_2B_6 after the initial lithiation process that remains inactive during cycling charge and discharge process. Moreover, obvious discharge and charge plateau at 0.45 V and 0.55 V that could be ascribed to the lithiation and delithiation reaction of MgH_2, respectively, are clearly observed for both bulk $Mg(BH_4)_2$ and $Mg(BH_4)_2$@G (Figures S18 and S19, Supporting Information). Therefore, it could be concluded that the lithiation and delithiation reaction of $Mg(BH_4)_2$ NPs results in the irreversible formation of $LiBH_4$ and Li_2B_6 during the initial discharge process and the reversible conversion of MgH_2 in the subsequent charge and discharge process. Interestingly, a stable cycling performance with a reversible capacity of 900 mAh g^{-1}, corresponding well with the theoretical capacity of MgH_2 that would be formed during the lithiation of $Mg(BH_4)_2$, could be well-preserved for $Mg(BH_4)_2$@G. This result directly demonstrates the excellent reversibility of MgH_2 that could be achieved during the charge and discharge process of $Mg(BH_4)_2$@G, which provides indirect evidence to the positive role of the formation of $LiBH_4$ and Li_2B_6 in promoting reversible charge and discharge process of MgH_2.

During the lithiation and delithiation process of MHG@MBH-13, the formation and irreversibility of Li_2B_6 during the initial discharge process could also be verified by XPS results (Figure 4c,d). It reveals the disappearance of B—H bonds of $Mg(BH_4)_2$ and the simultaneous formation of Li—B bonds of Li_2B_6 and Li—H bonds of LiH after the initial discharge process. Moreover, Li_2B_6 is well-preserved as the sole product after the reversible charge process with the almost complete absence of LiH, which not only confirms in situ formation of Li_2B_6 and hence $LiBH_4$ from the lithiation of $Mg(BH_4)_2$ covered on the surface of MgH_2 NPs, but also the reversible formation of MgH_2 that mainly accounts for the charge and discharge process of MHG@MBH-13. HRTEM images of MHG@MBH-13 after complete lithiation process (Figure 4e,f) exhibit distinct lattice fringe of 0.39, 0.34, and 0.42 nm, corresponding to the (112), (130), and (121) planes of in situ generated Li_2B_6 alloys, respectively. In addition, the lattice fringes of 0.21 and 0.15 nm, corresponding to the (110) and (200) planes of thus-formed Mg crystals, respectively, could also be detected. After the reversible delithiation process, the characteristic lattice fringe of MgH_2 could be clearly observed with the obvious presence of Li_2B_6 (Figure 4g,h), indicating the reversible formation of MgH_2 and the uniform preservation of Li_2B_6 around

© 2023 Wiley-VCH GmbH

16136829, 2023, 26, Downloaded from https://onlinelibrary.wiley.com/doi/10.1002/smll.202207210 by Fudan University, Wiley Online Library on [28/06/2023]. See the Terms and Conditions (https://onlinelibrary.wiley.com/terms-and-conditions) on Wiley Online Library for rules of use; OA articles are governed by the applicable Creative Commons License

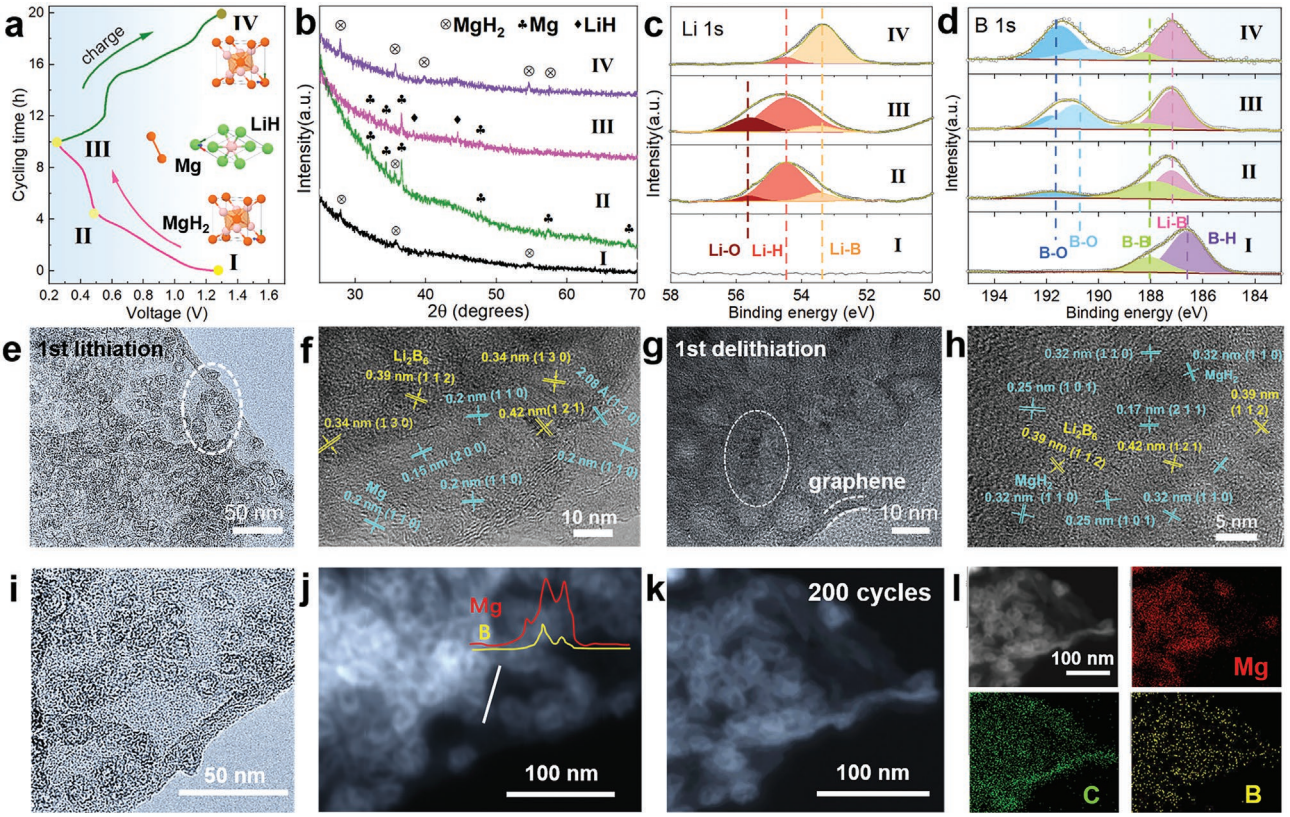

Figure 4. a) Evolution of the potential (V) along with cycling time for the MHG@MBH-13 electrode at 200 mA g^{-1} in the first cycle. b) XRD patterns and high-resolution c) Li 1s and d) B 1s XPS spectra of MHG@MBH-13 at different charge and discharge states. e,f) HRTEM images of MHG@MBH-13 collected at the first lithiation state and g,h) the delithiation state. i) TEM images and j) the EDS line scan on a STEM image of MHG@MBH-13 at the first delithiation state. k) STEM image and l) the elemental mapping of MHG@MBH-13 after 200 cycles at 2 A g^{-1}.

MgH_2. Based on the combination of HRTEM and XPS results, the initial delithiation process of MHG@MBH-13 results in in situ formation of Li_2B_6 and $LiBH_4$ covered on the surface of MgH_2 NPs, which, on one hand, could effectively prevent the agglomeration of MgH_2 NPs as evidenced by SEM (Figure S22, Supporting Information) and TEM (Figure 4i) images. Moreover, the elemental line-scan profiles on the single MH@MBH NP illustrate Gaussian distributions across the particle for the elements B and Mg, which confirms the uniform distribution of $LiBH_4$ and/or Li_2B_6 on the surfaces of MgH_2 NPs. STEM image and its corresponding elemental mapping results of MHG@MBH-13 (Figure 4k) verifies that the uniform distribution of MgH_2 NPs on graphene with an average particle size of ≈12.1 nm (Figure S24, Supporting Information) is well preserved at 2 A g^{-1} after even 200 cycles. By comparison, without the uniform coverage of $Mg(BH_4)_2$ layers, obvious agglomeration of MgH_2 NPs could be observed for MHG-13 after only 50 cycles (Figure S23, Supporting Information).

The interfacial contact between solid-state electrolyte and the electrode plays an important role in the electrochemical performance of ASSLIBs. Hence, the interface changes of between the electrode and the solid electrolyte upon cycling are visually investigated by cross-sectional SEM measurement and elemental mapping, which demonstrates that interfacial contact between MHG-13 and the solid electrolyte is comparable to that of MHG@MBH-13 electrode at the initial state (**Figure 5**a,b). After 200 cycles of repeated charge and discharge process, obvious interspace and gap could be obviously observed at the interfaces between MHG-13 and the solid electrolyte owing to the large volume change of MgH_2 and thus-generated phase separation. This phenomenon is aggravated upon further cycling and serious detachment and separation could even be observed at the electrode side, which results in poor interfacial contact that increases the electronic and ionic conductivity of the whole cells. As a result, the charge transfer resistance (R_{ct}) of the MHG-13 electrode is increased from 6.8 to 18.2 Ω after 200 cycles (Figure 5d,f). Moreover, the Li ion diffusion coefficient (D_{Li}) of MHG-13 electrode obtained from potentiostatic intermittent titration technique (PITT) is calculated to be 5.9×10^{-16} cm^2 s^{-1} at the initial state (Figure S25, Supporting Information) and this value is sharped decreased down to 8.8×10^{-17} cm^2 s^{-1} after only 20 cycles (Figure 5g). In strong contrast, the compact assembly at the interface between MHG@MBH-13 and $LiBH_4$ could be well-preserved during 500 cycles of discharge and charge process without the presence of obvious detachment as observed in the MHG-13 electrode, which could attributed to the suppressed volume change and phase separation of MgH_2 induced by the uniform coating of $Mg(BH_4)_2$ layers. More importantly, a gradual decrease of R_{ct} from 5 Ω to only 2.2 Ω after 200 cycles could be achieved for the MHG@MBH-13 electrode owing to the interface stability between MHG@MBH-13 electrode and the electrolyte (Figure 5c,e).

 © 2023 Wiley-VCH GmbH

16136829, 2023, 26, Downloaded from https://onlinelibrary.wiley.com/doi/10.1002/smll.202207210 by Fudan University, Wiley Online Library on [28/06/2023]. See the Terms and Conditions (https://onlinelibrary.wiley.com/terms-and-conditions) on Wiley Online Library for rules of use; OA articles are governed by the applicable Creative Commons License

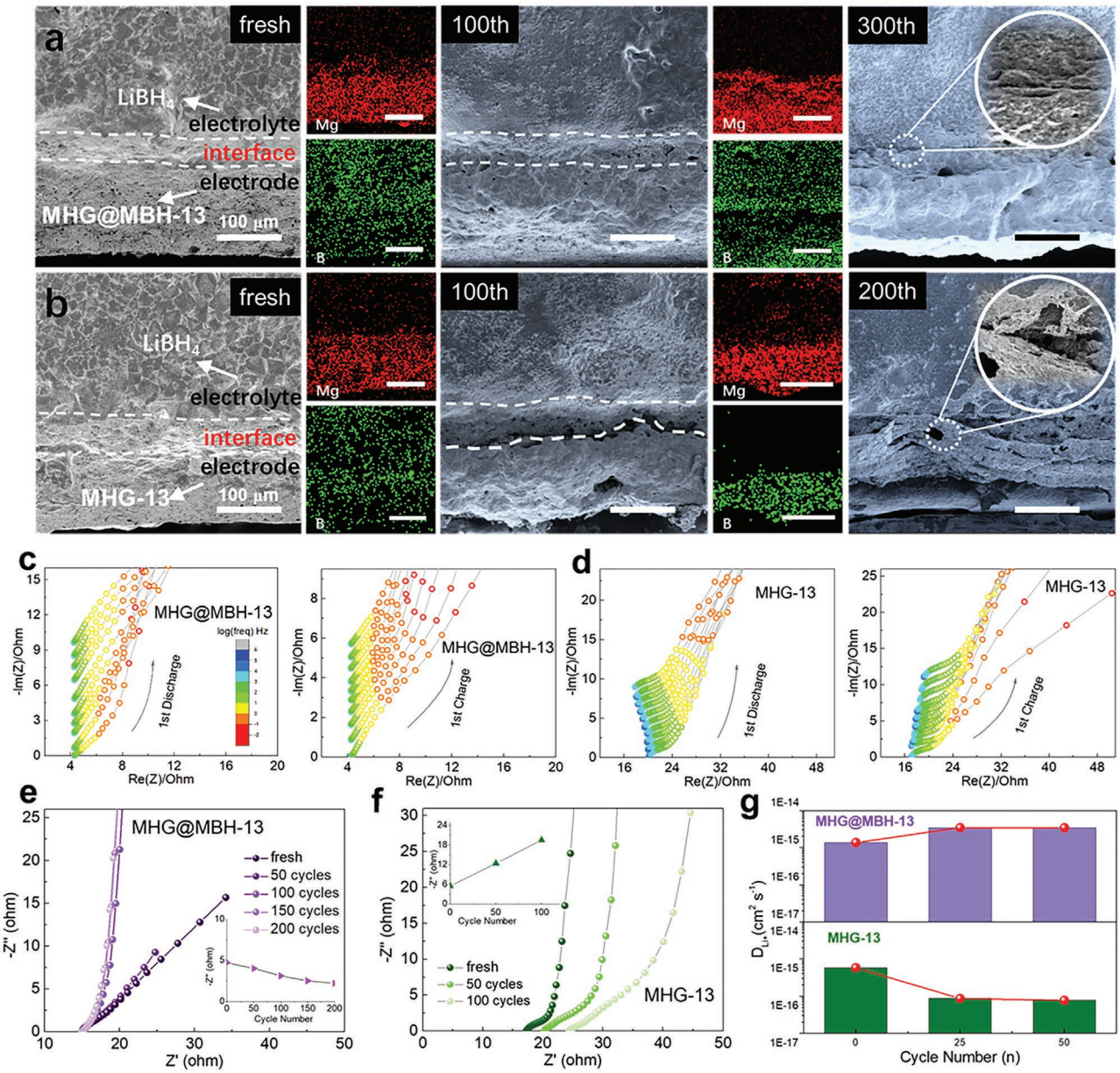

Figure 5. Cross-sectional SEM images of the interface a) between MHG@MBH-13 and the solid electrolyte and b) between MHG-13 and the solid electrolyte at the initial state and after various cycles at 2 A g^{-1}. Impedance measurement during the initial discharge and charge cycle for the as-synthesized c) MHG@MBH-13 and d) MHG-13 electrode. Nyquist plots of the as-synthesized e) MHG@MBH-13 and f) MHG-13 electrode during cycling. g) The comparison of the diffusion coefficient of MHG@MBH-13 and MHG-13 extracted from high resolution PITT characterization.

Impressively, the D_{Li} of the MHG@MBH-13 electrode reaches 1.5×10^{-15} cm^2 s^{-1} at 0.5 V, which is two orders of magnitude higher than that of the MHG-13 electrode (3.65×10^{-17} cm^2 s^{-1}) and the D_{Li} of MHG@MBH-13 during almost the whole charge and discharge steps is much higher than that of the MHG-13 electrode. It is noticed that there is a clear decrease of D_{Li} of MHG@MBH-13 electrode at ≈0.4 V during the discharge process. It could be attributed to the formation of B at this stage from the lithiation process of $Mg(BH_4)_2$, which would lead to the decrease of Li diffusion kinetics and then Li_2B_6 with high Li ion conductivity, which would enhance the Li ion diffusion kinetics of MHG@MBH-13 electrode. In addition, the structural change of MHG@MBH-13 induced the phase transformation of MgH_2 and $Mg(BH_4)_2$ could also lead to the change of Li diffusion kinetics. These results directly demonstrate the faster Li ions diffusion kinetics of MHG@MBH-13 electrode than that of MHG-13 electrode, which could be possibly attributed to the uniform formation of the $LiBH_4$ electrolyte on the surface of MgH_2 with intimate contact induced by the in situ discharge process of $Mg(BH_4)_2$ layers. Moreover, a slight increase of D_{Li} could be observed for the MHG@MBH-13 electrode after 20 cycles and the D_{Li} is maintained to be 3.5×10^{-15} cm^2 s^{-1} after 50 cycles, indicating that the high Li ions diffusion kinetics of MHG@MBH-13 electrode could be well preserved, which results in its excellent cycling stability.

 © 2023 Wiley-VCH GmbH

16136829, 2023, 26, Downloaded from https://onlinelibrary.wiley.com/doi/10.1002/smll.202207210 by Fudan University, Wiley Online Library on [28/06/2023]. See the Terms and Conditions (https://onlinelibrary.wiley.com/terms-and-conditions) on Wiley Online Library for rules of use; OA articles are governed by the applicable Creative Commons License

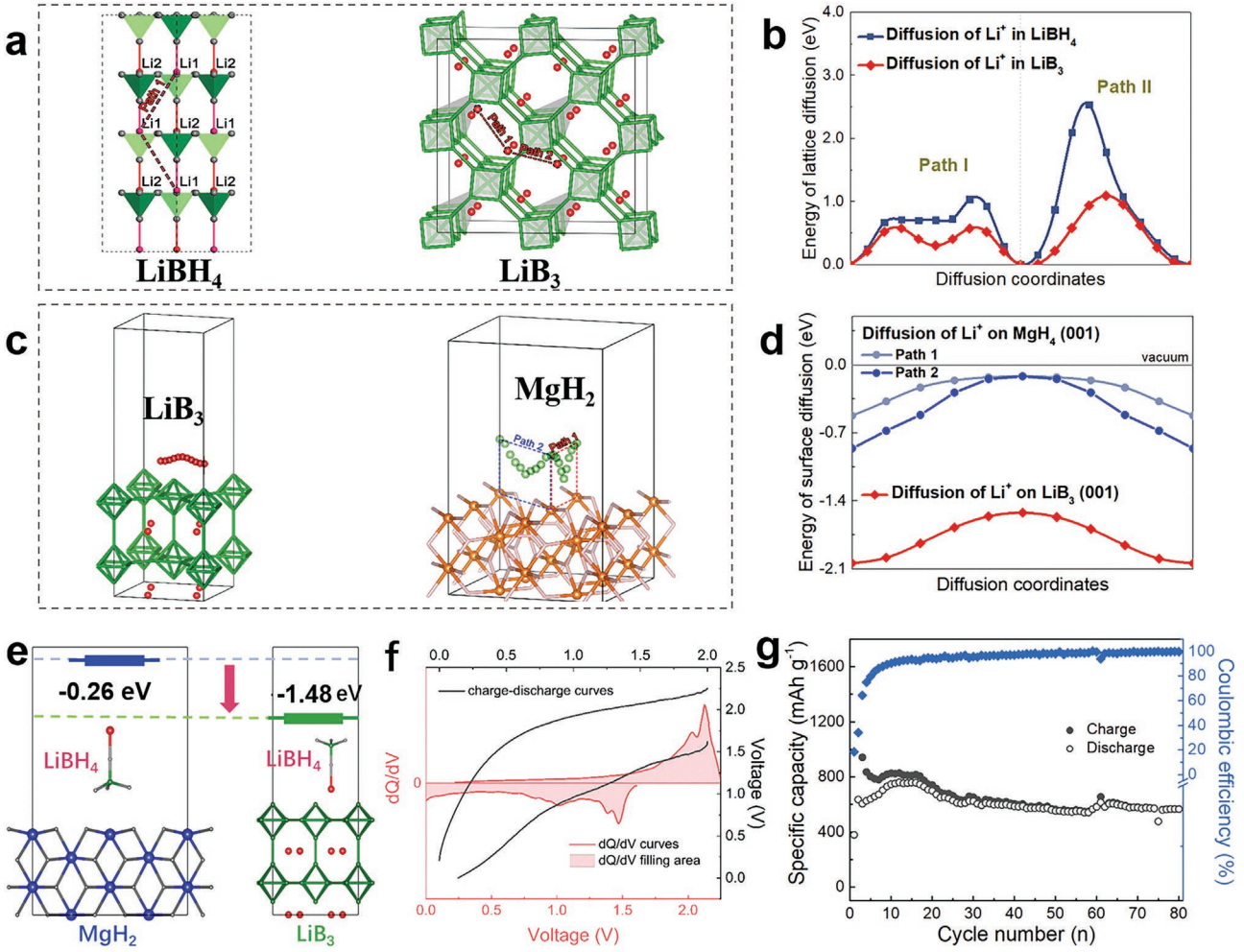

Figure 6. a) The diffusion paths of Li^+ inside of $LiBH_4$ (Path I) and LiB_3 between two equivalent sites and b) their corresponding energy profiles. c) The diffusion paths of Li^+ on the surface of MgH_2 (001) and LiB_3 (001) and d) their corresponding energy profiles. e) The comparison of the absorption energy profile between $LiBH_4$ molecular and MgH_2 (001) surface and LiB_3 (001) surface. f) The galvanostatic charge–discharge profiles and g) cycling performance of the assembled all-solid-state Li_2S//$LiBH_4$//MHG@MBH-13 full cells.

To deeply understand the effect of $Mg(BH_4)_2$ layers in improving the Li ion diffusion kinetics of MgH_2, theoretical calculations based on density functional theory (DFT) are performed. Interestingly, in comparison with $LiBH_4$ that serves as the solid-state electrolyte, the diffusion energy of Li in the lattice of Li_2B_6 that is in situ formed during the formation of $LiBH_4$ from the discharge process of $Mg(BH_4)_2$ layers is even much lower, indicating that Li_2B_6 is also a superior conductor of Li ions (**Figure 6**a,b and Figure S26, Supporting Information). In addition, the energy barrier for the Li diffusion on the surface of Li_2B_6 (001) is calculated to be 0.52 eV (Figure 6c,d), while this value reaches 0.73 eV on the surface of MgH_2 (001). These results demonstrate that the in situ formation of both Li_2B_6 and $LiBH_4$ that are uniformly covered on the surface of MgH_2 NPs facilitates fast transfer of Li ions from $LiBH_4$ electrolyte to the surface of the electroactive MgH_2. As a result, the D_{Li} of the MHG@MBH-13 electrode based on experimental observation is two orders of magnitude higher than that of the MHG-13 electrode (Figure 5g), which effectively promotes the electrochemical activity of MgH_2 NPs of MHG@MBH-13 electrode. Moreover, it is interesting to note that the absorption energy of $LiBH_4$ molecules on the surface of Li_2B_6 (001) approaches –1.48 eV while this value on the surface of MgH_2 (001) surface is only –0.26 eV (Figure 6e). This demonstrates strong capability of Li_2B_6 in the absorption of $LiBH_4$, which could not only stabilize the uniform coverage of in situ formed $LiBH_4$ on the surface of MgH_2, but also preserve the uniform distribution of $LiBH_4$ molecules around MgH_2 NPs during repeated charge and discharge process. Hence, the structural stability of MHG@MBH-13 electrode and the interface between MHG@MBH-13 electrode and the electrolyte could be well-preserved, which contributes to the excellent cycling stability of MHG@MBH-13. Such superior electrochemical properties of MHG@MBH-13 are among the best of MgH_2-based anode materials and compare favorably to the state-of-art values reported for all metal hydride-based anode materials (Figure 3g).

To evaluate the potential practical applications of MHG@MBH-13, all-solid-state full cells coupled with commercial Li_2S as the cathode material are assembled and tested. When using $LiBH_4$ as the solid electrolyte, an operating

 © 2023 Wiley-VCH GmbH

16136829, 2023, 26, Downloaded from https://onlinelibrary.wiley.com/doi/10.1002/smll.202207210 by Fudan University, Wiley Online Library on [28/06/2023]. See the Terms and Conditions (https://onlinelibrary.wiley.com/terms-and-conditions) on Wiley Online Library for rules of use; OA articles are governed by the applicable Creative Commons License

potential of 2.3 and 0.55 V could be observed for Li_2S and MHG@MBH-13 (Figure S27, Supporting Information), respectively. As a result, the all-solid-state full cells deliver an average discharge voltage of ≈1.5 V (Figure 6f), delivering a discharge capacity of 2039.3 mA g^{-1} based on the mass of MgH_2 inside of MHG@MBH-13. Cycling performance of the full cell at 0.15 C (1 C = 2038 mA g^{-1}) illustrates that a reversible specific capacity of 741 mAh g^{-1} could be maintained after 20 cycles (Figure 6g and Figure S28, Supporting Information) with a coulombic efficiency of 89%, which directly demonstrates the potential of MHG@MBH-13 as the high-performance anode material for ASSLIBs.

3. Conclusion

In summary, the homogeneous construction of ionic conductive pathways on single MgH_2 nanoparticle uniformly connected by electronic conductive graphene is realized by the uniform coverage of each MgH_2 NPs with ultrathin $Mg(BH_4)_2$ layers to improve the electrochemical activity of MgH_2 toward ultra-stable reversibility in ASSLIBs. The initial discharge process of ultrathin $Mg(BH_4)_2$ layers leads to the in situ formation of solid electrolyte $LiBH_4$ and Li_2B_6, which exhibits a Li ion diffusion barrier even lower than that of $LiBH_4$, uniformly covered on the surface of each MgH_2 NPs. As a result, the Li ion conductivity of graphene-supported MgH_2 NPs covered with ultrathin $Mg(BH_4)_2$ layers is two orders of magnitude higher than that without $Mg(BH_4)_2$ layers. In addition, taking advantage of the strong adsorption capability of Li_2B_6 toward $LiBH_4$, the thus-formed inactive Li_2B_6 and the uniform distribution of graphene, acting as the structural support role, not only alleviates the volume change of MgH_2 NPs but also stabilizes the intimate contact between $LiBH_4$ and individual MgH_2 NPs upon cycling discharge and charge process. On the other hand, the uniform distribution of MgH_2 NPs on graphene with high electronic conductivity increases the interfacial electronic conductivity of the whole electrode and meanwhile decreases the Li ion diffusion pathways for fast lithiation and delithiation. Consequently, the formation of stable interfaces that have high ionic and electronic conductivity is realized on the surface of each MgH_2 NPs. This proof-of-concept strategy in the rational design of stable interfaces with high ionic and electronic conductivity opens up new opportunities toward achieving the practical application of MgH_2-based electrodes in ASSLIBs.

Supporting Information

Supporting Information is available from the Wiley Online Library or from the author.

Acknowledgements

Y.H., P.G., and T.Z. contributed equally to this work. This work was partially supported by the National Key R&D Program of China (No. 2021YFB3802400), the National Natural Science Foundation of China (22279020,,51971065, 22109026), NSAF (Grant No. U2130208), the Science and Technology Commission of Shanghai Municipality (No. 21ZR1407500), and the Innovation Program of Shanghai Municipal Education Commission (2019-01-07-00-07-E00028).

Conflict of Interest

The authors declare no conflict of interest.

Data Availability Statement

The data that support the findings of this study are available in the supplementary material of this article.

Keywords

borohydrides, interfaces, ionic conductivity, metal hydrides, solid-state Li ion batteries

Received: November 19, 2022
Revised: February 12, 2023
Published online: March 21, 2023

[1] Y.-G. Lee, S. Fujiki, C. Jung, N. Suzuki, N. Yashiro, R. Omoda, D.-S. Ko, T. Shiratsuchi, T. Sugimoto, S. Ryu, J. H. Ku, T. Watanabe, Y. Park, Y. Aihara, D. Im, I. T. Han, *Nat. Energy* **2020**, *5*, 299.
[2] F. Zhou, Z. Li, Y.-Y. Lu, B. Shen, Y. Guan, X.-X. Wang, Y.-C. Yin, B.-S. Zhu, L.-L. Lu, Y. Ni, Y. Cui, H.-B. Yao, S.-H. Yu, *Nat. Commun.* **2019**, *10*, 2482.
[3] E. A. Wu, S. Banerjee, H. Tang, P. M. Richardson, J.-M. Doux, J. Qi, Z. Zhu, A. Grenier, Y. Li, E. Zhao, G. Deysher, E. Sebti, H. Nguyen, R. Stephens, G. Verbist, K. W. Chapman, R. J. Clément, A. Banerjee, Y. S. Meng, S. P. Ong, *Nat. Commun.* **2021**, *12*, 1256.
[4] X. Yang, Y. Hu, N. Dunlap, X. Wang, S. Huang, Z. Su, S. Sharma, Y. Jin, F. Huang, X. Wang, S.-h. Lee, W. Zhang, *Angew. Chem., Int. Ed.* **2020**, *59*, 20385.
[5] Y. Kato, S. Hori, T. Saito, K. Suzuki, M. Hirayama, A. Mitsui, M. Yonemura, H. Iba, R. Kanno, *Nat. Energy* **2016**, *1*, 16030.
[6] F. Han, A. S. Westover, J. Yue, X. Fan, F. Wang, M. Chi, D. N. Leonard, N. J. Dudney, H. Wang, C. Wang, *Nat. Energy* **2019**, *4*, 187.
[7] X. Fan, J. Yue, F. Han, J. Chen, T. Deng, X. Zhou, S. Hou, C. Wang, *ACS Nano* **2018**, *12*, 3360.
[8] B. Zahiri, A. Patra, C. Kiggins, A. X. B. Yong, E. Ertekin, J. B. Cook, P. V. Braun, *Nat. Mater.* **2021**, *20*, 1392.
[9] X. Fan, X. Ji, F. Han, J. Yue, J. Chen, L. Chen, T. Deng, J. Jiang, C. Wang, *Sci. Adv.* **2018**, *4*, eaau9245.
[10] Y. Oumellal, A. Rougier, G. A. Nazri, J. M. Tarascon, L. Aymard, *Nat. Mater.* **2008**, *7*, 916.
[11] Y. Pang, X. Wang, X. Shi, F. Xu, L. Sun, J. Yang, S. Zheng, *Adv. Energy Mater.* **2020**, *10*, 1902795.
[12] L. Zeng, T. Ichikawa, K. Kawahito, H. Miyaoka, Y. Kojima, *ACS Appl. Mater. Interfaces* **2017**, *9*, 2261.
[13] L. Zeng, K. Kawahito, S. Ikeda, T. Ichikawa, H. Miyaoka, Y. Kojima, *Chem. Commun.* **2015**, *51*, 9773.
[14] D. Meggiolaro, G. Gigli, A. Paolone, F. Vitucci, S. Brutti, *J. Phys. Chem. C* **2013**, *117*, 22467.
[15] L. Huang, L. Aymard, J.-P. Bonnet, *J. Mater. Chem. A* **2015**, *3*, 15091.
[16] P. Gao, S. Ju, Z. Liu, G. Xia, D. Sun, X. Yu, *ACS Nano* **2022**, *16*, 8040.
[17] F. Mo, J. Ruan, S. Sun, Z. Lian, S. Yang, X. Yue, Y. Song, Y.-N. Zhou, F. Fang, G. Sun, S. Peng, D. Sun, *Adv. Energy Mater.* **2019**, *9*, 1902123.
[18] F. Lu, Y. Pang, M. Zhu, F. Han, J. Yang, F. Fang, D. Sun, S. Zheng, C. Wang, *Adv. Funct. Mater.* **2019**, *29*, 1809219.
[19] H. Liu, Z. Ren, X. Zhang, J. Hu, M. Gao, H. Pan, Y. Liu, *Chem. Mater.* **2020**, *32*, 671.
[20] W. Yang, H. Liu, Z. Ren, N. Jian, M. Gao, Y. Wu, Y. Liu, H. Pan, *Adv. Mater. Interfaces* **2019**, *6*, 1801631.

 © 2023 Wiley-VCH GmbH

16136829, 2023, 26, Downloaded from https://onlinelibrary.wiley.com/doi/10.1002/smll.202207210 by Fudan University, Wiley Online Library on [28/06/2023]. See the Terms and Conditions (https://onlinelibrary.wiley.com/terms-and-conditions) on Wiley Online Library for rules of use; OA articles are governed by the applicable Creative Commons License

[21] L. Hu, H. Wang, Y. Liu, F. Fang, B. Yuan, R. Hu, *ACS Appl. Mater. Interfaces* **2022**, *14*, 1260.
[22] A. H. Dao, N. Berti, P. López-Aranguren, J. Zhang, F. Cuevas, C. Jordy, M. Latroche, *J. Power Sources* **2018**, *397*, 143.
[23] A. El Kharbachi, H. Uesato, H. Kawai, S. Wenner, H. Miyaoka, M. H. Sørby, H. Fjellvåg, T. Ichikawa, B. C. Hauback, *RSC Adv.* **2018**, *8*, 23468.
[24] B. Zhang, G. Xia, D. Sun, F. Fang, X. Yu, *ACS Nano* **2018**, *12*, 3816.
[25] G. Xia, B. Zhang, X. Chen, D. Sun, Z. Guo, F. Liang, W. Zou, Z. Yang, X. Yu, *ACS Nano* **2018**, *12*, 8177.
[26] B. Zhang, G. Xia, W. Chen, Q. Gu, D. Sun, X. Yu, *ACS Nano* **2018**, *12*, 12741.
[27] G. Xia, L. Zhang, X. Chen, Y. Huang, D. Sun, F. Fang, Z. Guo, X. Yu, *Energy Storage Mater.* **2018**, *14*, 314.
[28] G. Xia, Y. Tan, X. Chen, D. Sun, Z. Guo, H. Liu, L. Ouyang, M. Zhu, X. Yu, *Adv. Mater.* **2015**, *27*, 5981.
[29] H. Zhang, G. Xia, J. Zhang, D. Sun, z. Guo, X. Yu, *Adv. Energy Mater.* **2018**, *8*, 1702975.
[30] Y. Wang, X. Chen, H. Zhang, G. Xia, D. Sun, X. Yu, *Adv. Mater.* **2020**, *32*, 2002647.

 © 2023 Wiley-VCH GmbH

16136829, 2023, 26, Downloaded from https://onlinelibrary.wiley.com/doi/10.1002/smll.202207210 by Fudan University, Wiley Online Library on [28/06/2023]. See the Terms and Conditions (https://onlinelibrary.wiley.com/terms-and-conditions) on Wiley Online Library for rules of use; OA articles are governed by the applicable Creative Commons License